

Electrochemical behavior of a Magnesium ZK60 alloy processed by high-pressure torsion

Hamidreza Torbati-Sarraf^{1,*}, Seyed Alireza Torbati-Sarraf²,

Amir Poursaei^{1,3}, Terence G. Langdon^{2,4}

¹ Glenn Department of Civil Engineering, Clemson University, Clemson, SC 29634, USA

² Departments of Aerospace & Mechanical Engineering and Materials Science,
University of Southern California, Los Angeles, CA 90089, USA.

³ Department of Materials Science and Engineering, Clemson University, SC 29634, USA

⁴ Materials Research Group, Department of Mechanical Engineering,
University of Southampton, Southampton SO17 1BJ, UK

*Corresponding author. E-mail address: storbati@clemson.edu

Abstract

High-pressure torsion (HPT) was used to evaluate the effect of straining on the electrochemical properties of a ZK60 magnesium alloy. The samples were processed using HPT up to 20 turns and the electrochemical responses were examined through polarization, EIS, Mott–Schottky and hydrogen evolution tests. Electron back-scatter diffraction (EBSD) studies showed more homogeneity with finer average grain sizes accompanied by the evolution of a nobler texture when increasing the numbers of HPT turns. Ultimately, this led to improved corrosion behavior for the HPT-processed disks. Post corrosion observations revealed improved protective layers after higher turns of HPT.

Keywords: HPT, Magnesium ZK60, Corrosion, polarization, Mott-Schottky

1. Introduction

Magnesium alloys are desirable choices as lightweight materials for energy or fuel conservation and biomedical applications; Nevertheless, the main factors currently limiting a wider use of Mg products are the difficulties in processing these alloys, the relatively low strength and ductility, and the extremely high reactivity and poor corrosion resistance in various working environments [1-3]. Recent studies attempted to address these difficulties with the objective of improving either the mechanical or the corrosion properties but relatively few studies have considered the mutual impact of these properties on each other [4]. In practice, both of these properties are linked to the alloy composition and microstructure and this originates from the manufacturing process [5] and therefore needs to be considered synergistically.

Severe plastic deformation (SPD) is an effective method for improving the mechanical properties of Mg alloys. Processing by SPD causes grain refinement, a redistribution of solutes and changes in the crystallographic orientations within the microstructure which may also have a significant impact on the corrosion properties. To date, there are number of recent studies examining the influence of SPD processing on the corrosion behavior of Mg and its alloys [5-12]. Theoretically, the grain boundaries appear more active than the bulk, therefore, grain refinement leads to a more susceptible surface [13]. However, other modifications such as the grain size distribution [14] and the evolution of anisotropic texture [5,11,12,15,16] may also occur simultaneously with the grain refinement and this may play a more critical influence on the corrosion behavior of the Mg alloys.

The deformation capabilities of Mg alloys through conventional processing are poor due to their hexagonal close-packed (HCP) structure and this means that the processing is generally conducted at relatively high temperatures. However, high-pressure torsion (HPT) is an SPD

process that has an established capability in producing significant grain refinement in a range of Mg alloys and, more important, the processing can be effectively conducted at room temperature without the development of segmentation or cracking in the base metal [17,18]. Although the effect of various SPD processes on corrosion of magnesium was investigated thoroughly [5,6,8,12,19-21], nevertheless little attention was devoted to the development of electrochemical behavior in the HPT-processed Mg alloys [9,10,22-24] where reports have centered mainly on noting that more refined grains lead to a more homogenous corrosion. In practice, processing by HPT permits a study of corrosion behavior over a wide range of grain sizes and grain size distributions [25,26].

Earlier investigations of authors on the ZK60 Mg alloy showed that HPT induced an inhomogeneous strain along the radius of samples by torsional straining and, as a result, the average grain size and the mechanical properties tended to vary along the radius of the samples but an almost homogeneous microhardness distribution with finer grain size and reasonable uniformity was attained after higher numbers of HPT turns [27-29]. The mechanical and thermal stability behavior of ZK60 after HPT was evaluated recently by the current authors [30,31] but it is imperative to study the electrochemical behavior of the refined ZK60 alloy. Accordingly, this research was initiated to assess the electrochemical and semiconductive oxide layer behavior of the ZK60 Mg alloy after processing through HPT with different numbers of turns and to make a direct comparison with the behavior of extruded material.

2. Experimental material and procedures

A commercially available ZK60 magnesium alloy with a composition (in wt.%) of 5.5 % Zn, 0.5 % Zr was used in this study in the form of extruded rods. The rods with diameters of 10 mm were sliced into disks having thicknesses of approximately 1.2 mm and then both sides of

each disk were abraded with SiC papers to achieve smooth surfaces with uniform final thicknesses of approximately 0.8 mm.

2.1 HPT processing

The HPT processing was conducted using a facility with a rotating lower anvil and stationary upper anvil and the experiments were carried out under quasi-constrained conditions [32]. The torsional strain was applied to the disks by rotating the lower anvil under an applied pressure of 2.0 GPa at a constant speed of 1 rpm. The HPT-processed disks were prepared through total numbers, N , of 1, 2, 5, 10 and 20 turns. Post-inspection of the processed disks revealed no cracking or signs of damage by HPT processing.

2.2 Electron back-scatter diffraction (EBSD) sample preparation

Samples were prepared for electron back-scatter diffraction (EBSD) with a JEOL IB09010CP ion beam cross-sectional polishing machine for 5 h at an operating voltage of 6 kV. A scanning electron microscope (SEM) JEOL JSM-7001F was used at an operating voltage of 7 kV and orientation imaging microscopy (OIM) was employed to record the experimental data. A minimum of 2000 grains was examined for measurements of the average grain size and the grain size distributions. In subsequent descriptions, ND, RD, and TD correspond to the Normal Direction (torsion axis), Radial Direction, and Tangential Direction, respectively. The crystallographic plane of $\{0001\}$ in the EBSD images was used to evaluate textural evolutions of the materials with the pole figures. The EBSD images were recorded from the semi-oval areas of samples in the mid-radius of the TD-RD plane at the near surface position of the disks. Earlier studies provide a more detailed description of the sample preparation for EBSD [33,34].

2.2 Electrochemical testing

All of the electrochemical tests were carried out at room temperature in a 0.1 M NaCl aqueous solution. Prior to exposure to the solution, samples were sequentially wet ground with 800 and 1200-grit SiC abrasive papers, washed with distilled water and alcohol and then dried immediately. A Saturated Calomel Electrode (SCE) and a platinum mesh were used as the reference and the counter electrodes, respectively. Extruded and HPT processed samples were used as the working electrode.

To establish the electrical connection for electrochemical tests, wires were glued to one side of each processed disk. In order to conduct overall examination on the electrochemical behavior of ZK60 Mg alloy processed with different number of HPT turns, the whole surfaces of the samples were exposed to the solution. Therefore, the edges, back side and the connection were coated with epoxy to minimize any undesirable effects. To achieve a quasi-steady open circuit potential (OCP), the samples were immersed in the solution for approximately 200 minutes. Then, electrochemical impedance spectroscopy (EIS) was performed with a sinusoidal potential amplitude of 5 mV versus the OCP over the frequency range of 100 kHz to a few mHz. At 30 minutes after the EIS test, potentiodynamic polarization was carried out over a potential range from -2.0 V to 0 V versus SCE with a scan rate of 1 mV/s.

In order to assess the semiconductive and the capacitive behaviors of the oxide layer formed on the surface of the disks, the same sample from the polarization test was again ground and prepared for OCP and EIS similar to the earlier procedure and afterwards the Mott–Schottky test was carried out on the sample by employing staircase potential electrochemical impedance spectroscopy (SPEIS) with 5 mV AC perturbation at selected frequencies from 100 kHz to 100 Hz in a variable potential from -2.0 to -1.6 V vs SCE during a 10 mV/s scan rate. Basically, the time of immersion was selected based on the results of the hydrogen evolution test.

2.3 *Hydrogen evolution testing*

Quasi-steady behavior in the H₂ evolution was observed after about 4 hours immersion in the solution as will be discussed later. Under OCP conditions, the corrosion rate can be measured from the rate at which H₂ evolution occurs on the corroding surface [35]. The collection of hydrogen gas is widely used to evaluate Mg alloys corrosion rate [4,36-38]. The H₂ gas bubbles produced as a result of the dissolution of Mg are collected with an inverted funnel inside the solution and conveyed to a volumetric burette [35]. Therefore, the volumetric measurement of the evolved hydrogen gives good trend for measurement of the weight loss of the metal [39]. However, for low rates of corrosion, as in the case investigated in this study with relatively mild corrosivity, this technique tends to underestimate corrosion rate [40]. Consequently, in this study, the volume of evolved hydrogen obtained from direct measurements was used to monitor and compare the activity of HPT processed samples with different numbers of turns during 24 hours. In this experiment, the whole surface of disk-shaped extruded and HPT samples, with diameters of approximately 10 mm, were immersed in the solution with a volume per unit surface area of 100 ml.cm⁻².

The surfaces of the samples after 4 hours exposure to the solution were observed using an optical microscope with images taken from different locations and then positioned together in order to form a complete image of the sample. This procedure was repeated for 10 and 24 hours of immersion to provide a pictorial presentation of the corrosion process over the total exposure time. Ultimately, the corroded surfaces after 24-hour exposure were examined and the morphology and composition of the surfaces were analyzed with scanning electrochemical microscopy and energy dispersive spectroscopy (EDS). In order to achieve reliable reproducibility of the measurements, all of the electrochemical tests were conducted on three different samples.

3. Experimental results

3.1 *Effect of HPT processing on microstructural and textural evolution*

EBSD analysis provides an overall evaluation of grain size and grain size distribution during the HPT process. A summary of the analysis with examples of OIM maps are configured in Figure 1. All the data were obtained from the mid-radius of each disks including the unprocessed condition and after processing by HPT through 1 and 5 turns.

It is apparent from these results that processing by HPT reduces the grain size from an initial value of several microns to a final average value of ~700 nm after processing for 5 turns. It should be noted that further EBSD analysis with even more HPT turns was not possible due to the extreme deformation imposed on the samples after 10 and 20 turns. Thus, samples with high numbers of HPT turns hardly revealed any Kikuchi bands and consistently exhibited a low confidence index (CI) for visualization of the microstructure in the EBSD images.

Observations of the microstructural evolution during HPT processing revealed that the grain size distribution stretched over one order of magnitude of the grain size for all experimental conditions. Nevertheless, there is a gradual decrease in the average grain size values by increasing the number of HPT turns. These observations were extensively described for the same processed materials in earlier studies of the grain size evolution with bimodalities in the grain size distributions in ZK60 Mg alloys processed by HPT [18,27,28,41].

In practice, the grain size and the texture both change with straining of the material. The pole figures obtained from $\langle 0001 \rangle$ crystallographic orientation are shown in Figure 2 for the extruded condition and after 1 and 5 turns. By increasing the number of HPT turns, a gradual change towards basal planes, $\{0001\}$, is evident with the c-axis parallel, or close to parallel, to the normal direction to the torsion axis or the surface exposed to the corrosive environment. This result

is consistent with the earlier studies of the texture behavior of HPT processed ZK60 Mg alloy with XRD method [41].

3.2 Electrochemical testing of HPT-processed materials

The potentiodynamic polarization curves of the extruded and HPT processed samples after ~4 hours of immersion in a 0.1 M NaCl solution are shown in Figure 3. It is readily apparent that the stages of the cathodic reactions, with hydrogen evolution as the main reaction, are very similar for all samples up to and including 20 turns and thus there is no significant influence of the HPT process on the kinetics of the cathodic reactions at high cathodic overpotentials [43]. However, the E_{corr} values of the HPT processed samples are ~100-150 mV which is more noble than the extruded sample, presumably due to the formation of a nobler crystallographic texture towards the basal planes [5,8,11,44] after HPT processing. Nevertheless, E_{corr} does not change significantly by increasing the numbers of turns from 5 through to 20. The kinetics of the anodic dissolution of the HPT-processed samples showed inconsistent behavior because for 1 and 2 turns the anodic current increased with an increase of potential whereas for 5, 10 and 20 turns there were apparent pseudo passive window trends. This behavior is attributed to the formation of partially protective corrosion products on the surface of disks [5,11,45]. This potential increased with the increase in the number of turns, showing an enhancement in the adhesion and protectiveness of the film formed on the surface of the ZK60 alloy by increasing numbers of turns during HPT. However, with the potential increment, the quasi-protective film is prone to lose its integrity and break down and subsequently it is expected that the current density starts to increase, thereby implying the free dissolution of Mg and the evolution of H_2 bubbles [39,43,46,47].

A reliable analysis of the corrosion of Mg and its alloys by conventional DC electrochemical methods, such as with polarization, requires both half-cell reactions are controlled

by activation polarization [37]. In studies of the corrosion of Mg alloys, hydrogen evolution occurs through both anodic and cathodic polarizations which increase the ohmic potential and makes it difficult to compensate [36,48]. In addition, except in activation-controlled kinetics, polarization curves do not show linear behaviors which makes it more difficult to conduct and comprehend the analysis [49,50]. Furthermore, the products formed on the surface during corrosion may lead to significant deviations in the reactions from the OCP [39,50-52]. Thus, in studying the corrosion of Mg alloys, instant corrosion rate determinations using the DC electrochemical method is difficult and should be accompanied by an AC electrochemical technique and a non-electrochemical technique such as a hydrogen collection method [35,52,53].

The Nyquist spectra obtained from the EIS experiment for one of the samples of each group in a 0.1 M NaCl solution are shown in Figure 4. All EIS spectra contain one high and one medium frequency capacitance loop and one inductive loop at the low-frequency. Evidently modification of the impedance with increasing the turns of HPT can be attributed to the improvement and integrity of the MgO/Mg(OH)₂ oxide layer [52-55]. The corrosion of magnesium in an aqueous solution can be described by the following net reactions [46,51,56,57] shown in Eq. 1-4:



The relaxation processes of adsorbed species, $\text{Mg}(\text{OH})_2$, cause the formation of the inductive loop at the low-frequency domain [51,53,55]. The mass-transport loop, second capacitance loop, in the medium-frequency range is attributed to the diffusion of Mg^{2+} through the porous $\text{Mg}(\text{OH})_2$ corrosion product layer which is not compact but covers entirely the surface and allows easy penetration of aggressive ions [54,58]. Subsequently, the inner oxide layer composed of MgO is formed progressively in equilibrium as follows [54,56]:



which appears in the high-frequency (HF) capacitive loop as a result of both charge transfer and film effect [52,54,55,58,59].

Based on the described proposed mechanism which also observed in other studies [54,58,60,61], an equivalent electrical circuit, shown in Fig 5, is used to elaborate the interface interaction. R_s corresponds to the solution resistance and was placed in series with all other elements. Since Mg dissolution mostly occurs at the film-free or porous areas [54,58], then a faradaic impedance, Z_F , in parallel with the double layer capacitance, C_d , ascribes production of Mg ions and the precipitation of a $\text{Mg}(\text{OH})_2$ porous layer. In parallel, C_f and R_f are attributed to the MgO inner oxide film capacitance and resistance, which are assumed to be very protective compared to the outer $\text{Mg}(\text{OH})_2$ layer [54]. R_f is depicted by a dashed line since it has no sensitive impact on the low frequency faradaic impedance. Therefore, R_f can be placed equal to the high frequency impedance part of the Nyquist, $R_{HF} \approx R_f$ [55,60].

The obtained Nyquist spectra are not perfect semicircles and cannot be used for direct determination of the capacitive behavior of the corroded surfaces. This imperfection in the Nyquist

spectra is attributed to the electrode geometry, inhomogeneity in microstructure, reactivity and resistivity in length of the adsorptive and oxide layer. As a result, using a constant phase element (CPE) is a proper approach to the non-ideal capacitances [58, 62-65].

The capacitance of an oxide film can be graphically determined by extrapolating the high frequency real capacitance, $C_f \approx C_{HF}$, using the Cole-Cole capacitance representation [52,66,67].

A complex capacitance can be calculated directly using Eq. 6:

$$C(\omega) = \frac{1}{j\omega(Z(\omega) - R_s)} \quad (6)$$

where, $j^2 = -1$ and ω is angular frequency [66]. R_s can be accurately obtained by extrapolation of the Nyquist plots with Z_{re} axis at high-frequencies [68]. Figure 6 shows the complex capacitance plots obtained from the EIS data. Applying the HPT process changes the behavior of the oxide film formed on the samples. Evidently, 1 and 2 HPT processed samples are more responsive to higher frequencies compared to the other samples, indicating CPE behavior along the surface due to the surface heterogeneity and geometrical effects [58]. The values of R_f and C_f obtained by the graphical method are given in Table 1. Although, this methodology yields a slight overestimation of the capacitance values [52,66,69], it provides a qualitative comparison. By applying the HPT processing, the film resistance increases in the order of $1 < 2 < 5 < \text{Extruded} < 10 < 20$ HPT turns. However, the C_f values show a different trend. By applying HPT, C_f first decreased and then gradually increased by a number of HPT turns. Assuming that the oxide film thickness is proportional to the reciprocal of the capacitance ($1/C_f$) of the oxide film [66], the trend obtained implies that applying the HPT forms a thicker oxide film on the surface of the electrode; but it becomes thinner by increasing turns of HPT.

It is hypothesized that the protective oxide film is not able to continuously cover the entire surface due to the small Pilling-Bedworth ($PB < 1$) ratio for MgO [37,52]. In addition, the presence of Cl^- ions in solution makes the surface susceptible to localized attack. Hence, despite the formation of a thicker oxide film on the HPT-processed samples with small numbers of turns compared to the other sample, this oxide film does not provide continuous coverage and resistance on the entire surface and leads to the formation of micro-galvanic cells between the covered and uncovered areas. Accordingly, the introduction of grain refinement through the initial turns of HPT generally reduces the corrosion resistance compared to the extruded sample. However, increasing the numbers of turns of HPT improves the corrosion resistance through the formation of a modified and integrated MgO film. This trend is consistent with increasing impedance of the oxide film and the pseudo-passive potential behavior observed at the polarization curves.

Electronic properties of the oxide film formed on Mg interface has significant role on its corrosion performance [70]. Charge carriers in the formed oxide film have different electrochemical potentials with respect to the solution [71], and this creates a space charge layer with a capacitance at Mg interface. The charge carrier density (N_q) of the oxide film can be extracted using Mott-Schottky equation:

$$\frac{1}{C^2} = \pm \frac{2}{\epsilon \epsilon_0 e N_q A^2} \left(V - V_{fb} - \frac{kT}{e} \right) \quad (7)$$

where ϵ is the dielectric constant of the corrosion products (for MgO this value is ~ 9.62), ϵ_0 represents the permittivity of vacuum (8.854×10^{-14} F/cm), A is the area of the exposed surface, V is the applied potential, V_{fb} is the flat band potential, e is the charge of the electron (1.602×10^{-19} C), k is Boltzmann's constant (1.38×10^{-23} J/K), T is the absolute temperature (298 K) [73-75]. The interfacial capacitance, C , can be equaled to space charge capacitance of oxide film by

neglecting capacitance of Helmholtz layer which is generally one order of magnitude higher than C_{ox} [55,60,70].

To ascertain the formation of a continuous oxide layer and make comparison with EIS data in OCP, prior to conducting the Mott-Schottky tests, samples were exposed in the 0.1 M NaCl solution for 4 hours immersion. As discussed earlier, CPE was observed in the dielectric properties of the oxide film. As a result, capacitance and accounted charge carrier density may also vary with the frequency. Nonetheless, applying multi-frequency capacitance measurements at relatively high frequencies ($f > 100\text{Hz}$) and high scan rate (10 mV/s) and extrapolating equivalent film capacitance provide precise calculation for Mott-Schottky plot [72]. Therefore, EIS spectra were analyzed for certain steps of potential and C values were graphically estimated with the same procedure explained for calculating the C_f . Mott-Schottky plots were created by plotting C^{-2} versus potential changes as shown in Figure 7. All samples exhibit positive slopes over a range of scanning potential and it indicates characteristics of n-type semiconductors with dominant defects of oxygen vacancies and/or metal cation interstitials [76]. By further increasing the potential, as already shown [70,74], the strength of the oxide film was weakened by hydrogen ionization which generated magnesium vacancies and led to a p-type semiconducting behavior. This behavior is consistent with the polarization curves where increasing turns of HPT forms a more resistive oxide film against an overpotential.

The donor densities of the oxide films, MgO, formed on the samples in the 0.1 M NaCl solution were calculated through slopes of the linear portions of the Mott-Schottky plots and substituting in derivative format of Eq (7) as shown in Figure 8. The donor densities of the HPT-processed samples with 1, 2, and 5 turns increase compared with the extruded sample whereas the donor densities of the HPT-processed samples with 10 and 20 turns are slightly less than for the

extruded sample. This behavior corroborates the EIS results, although the thickness of oxide film decreased with increasing numbers of turns, but the oxide becomes more integrated and less defective. It is noteworthy to mention that a quantitative estimation of the capacitance and charge carrier densities in the Mott-Schottky test may be affected by the localized electronic states [77], potential scan rate, the CPE behavior of electrode and neglecting Helmholtz layer [52]; therefore, the presented data were implemented to provide a more qualitative comparison by keeping all the test parameter constant and evaluating the effect of number of HPT turns.

3.3 Hydrogen evolution testing of HPT-processed materials

The results of the hydrogen evolution test are presented in Figure 9 for a 24 hours immersion in the 0.1 M NaCl solution at room temperature. In general, hydrogen evolution from a corroding surface at its OCP implies an electrochemical activity of the surface [35,40]. The cumulative amount of the volume of hydrogen gas evolved from the surface of the samples varies significantly with the numbers of turns and the results demonstrate that HPT changes the activity of the ZK60 alloy. In all cases, the total evolved hydrogen increases within almost the first four hours of exposure. This increment is significant for samples processed through 1, 2 and 5 turns, with 1 representing the highest and 5 the lowest. After around 4 hours, the rate of hydrogen evolution decreases with a decrease in the slope of the lines, thereby indicating the formation of partially protective corrosion products on the surface which reduce active surface area and hinder the dissolution [52,54]. The hydrogen evolution on the samples processed through 10 and 20 turns is much lower compared to the other HPT-processed samples. After 24 hours of immersion in the NaCl solution, the amount of hydrogen gas evolved on the surface of the HPT-processed sample after 20 turns was less than ~20% of that evolved on the HPT-processed surface for 1 turn, indicating a significant reduction in corrosion activity on that sample.

3.4 *Post-exposure microstructural observations*

The corresponding images obtained at different times of immersion in 0.1 M NaCl solution are shown in Figure 10. The disks generally corroded steadily due to the existence of chloride ions in solution, but from the extruded sample to the sample processed with 1 turn there is a degradation of material even after only 4 hours of exposure to the 0.1 M NaCl solution. The corrosion started generally from the periphery of the sample where there is maximum strain and consequently localized grain refinement as reported previously for this material by the co-authors of this study [27,30,41]. This trend can be observed in the higher magnification from a slice of disks in Figure 11. By increasing the numbers of turns, as demonstrated also in the results of the electrochemical tests and the hydrogen evolution experiments, the corrosion is ameliorated. The surface of the HPT-processed sample with 20 turns was corroded more homogeneously. A drastic increase in corrosion activity of the samples within the first four hours of immersion in solution and then a gradual increase after that time was also observed and this is also consistent with the results from the hydrogen evolution test. Nonetheless, by comparing images of the extruded disk with 4 hours immersion in Figure 10 with different times of immersion for 10 and 24 hours, it is concluded that the corrosion morphology and propagation path are not changed by the increasing time of immersion. By contrast, and for all HPT-processed samples, the morphology changes with time since more portions of the surface are covered by a corrosion product layer with darkish contrast. This behavior is also apparent in Figure 9 since the extruded sample shows a relatively constant rate of hydrogen evolution.

Figure 12 gives the corresponding images obtained at the mid-radius of each sample shown in Figure 10 at a higher magnification after 4 hours of immersion in the 0.1 M NaCl solution. Fundamental studies on the nature of the grain boundaries showed that, by comparison with the

crystal interior, the grain boundaries have relatively wider distributions of interatomic spacing with reduced atomic density due to the misfit between adjacent crystals and therefore the grain boundaries are more active regions compare to within the grains [78-80]. Accordingly, it is expected that chloride ions initially selectively attack such active regions [13,81]. For the extruded sample with conventional grain size, it is reasonable to expect that the majority of corrosion pathways are the grain boundaries, due to similarity and size of grains and boundaries between Figure 1 and Figure 12 for extruded samples. In the HPT-processed samples with 1, 2 and 5 turns, these paths expand but are not uniform due to incomplete grain refinement as shown in Figure 1 and were extensively discussed in a previous publication [27,29]. Consequently, a micro-galvanic corrosion between the interiors of the large grains and non-distorted areas as cathode with cluster of distorted grains with high boundary densities as anode can form [5,13]. Convection at the vicinity of this area, due to the copious hydrogen bubbling [43], can exacerbate corrosion. Therefore, at the early stages of HPT, partial grain refinement and the formation of an unintegrated and defective corrosion product film is barely beneficial and even accelerates the localized corrosion compared to the extruded ZK60 alloy. However, by increasing the numbers of HPT turns, the corrosion performance of the samples is improved, and this can be attributed to the more uniform grain refinement and grain distribution in these samples compared to the other samples as shown in the electrochemical results and micrographs in Figure 10 and 11. The uniform grain refinement in the HPT-processed samples with higher numbers of turns minimizes the occurrence of the micro-galvanic cells, enhances the stability of product film and ultimately leads to an improved corrosion behavior. Suffice to mention that, as Figure 11 shows and previously elaborated by authors [27], gradual grain refinement through HPT process is not homogenous along the radius of HPT disks for Mg alloys. Necklacelike configurations with small grains

surrounds the larger grains [18], although this grain refinement evolution is not practically proportional with radius at all regions, but microstructure evolves and becomes gradually homogenous by increasing numbers of turns. In the test solution of this study, explained micro-galvanic current restrict to current flux between nearby anodes and cathodes, and galvanic effect between each point across whole area of diameter are not addressed.

The SEM micrographs in Figure 13 with the corresponding EDS results from marked points provided in Table 2 show the microscopic morphologies of the extruded and the HPT-processed ZK60 disks after 24 hours immersion in the 0.1 M NaCl solution. The earlier observations in Figure 12 and deep concavity along this path at Figure 13 confirm that the dissolution mainly starts along this paths. The micrograph in Figure 13(a) and corresponding EDS in Table 2 demonstrate no discernible thick precipitate within the grain. However, Figure 13(b) and the corresponding EDS data in Table 2 show that localized corrosion and precipitate was detected mostly in the vicinity of fine grains with the presence of more Cl, presumably as $MgCl_2$ [4], and this corroborates the catalytic effect of these corrosion precipitates product in the form of pitting of this region [43]. By increasing the numbers of HPT turns those corrosion path and morphology observed for extruded and early stages of HPT processed samples, seems to be disappeared. In addition, as the composition analysis at point C implies, those corrosion product precipitates layer has relatively more oxide and less Cl^- ion and consequently less defective sites than for the 1 turn HPT sample. It is noteworthy that in the early stages of HPT isolated precipitates in the refined grain zones are fragmented due to the internal stresses of vigorous dissolution and corrosion precipitates accumulation. Thus, during immersion a localized corrosion accelerated by these precipitate peeling-off and the consequent penetration of an active aggressive Cl^- ion. By increasing the numbers of turns, the covered surfaces become more integrated and refined and

cracks disappear due to the homogenous formation of less defective corrosion products on uniformed grain refined substrate. The increasing R_f values is additional evidence of the higher protective properties of the oxide film after larger numbers of turns of HPT.

It should be noted that in this study a 0.1 M Cl^- , with relatively high ohmic resistance, was used as the aggressive ion whereas earlier research involved more corrosive environments such as 0.62 M $[\text{Cl}]^-$ (3.5 wt% NaCl) which may persistently attack the surface and break down and change the chemistry corrosion product [9,10,13,43]. On the other hand, using passivating rather than corrosive solutions such as a simulated body fluid leads to an improvement in the protective oxide layer and corrosion behavior in each turn of the HPT process compared both to earlier turns and to the original extruded condition [22,23,82].

4. Discussion

The poor corrosion resistance of Mg and its alloys mainly originates from two factors: first, the comparatively high electronegative potential of Mg which enables corrosion activity even without presence of oxygen. The second factor suggests that oxide/hydroxide layers that form on the surface of Mg are soluble in most aqueous environments and provide insufficient protective properties [1] and potentially accelerates corrosion [39,43,83]. The grain boundaries, inclusions and the defects are more active regions compared to the other grains and generally it is expected that the chloride ions will selectively attack these active regions first and accelerates dissolution [38-40,81].

The HPT processing imposes a torsional strain which varies across the disk radius. The equivalent von Mises strain describes the strain variation by number of turns of HPT, N .

$$\varepsilon_{eq} = \frac{2\pi Nr}{h\sqrt{3}} \quad (8)$$

where r is the radius and h is the thickness of the disk. Following Eq. (8) implies that ε_{eq} varies from zero at the center of the disk to a maximum at the edge [84,85]. It may be hypothesized that the significant increase in corrosion activity in the early stages of HPT processing originates from the variation of the imposed strain across each circular disk from zero at the center to a maximum at the periphery since this variation leads to an inhomogeneity in the refined grains [18,86]. Furthermore, this inhomogeneity in return causes the formation of isolated and broken surface precipitates on the HPT-processed samples which accelerate localized corrosion.

Partial grain refinement and non-protective corrosion product accumulation cannot be beneficial in enhancing the corrosion resistance of the extruded ZK60 alloy in the 0.1 M NaCl solution. However, by increasing the numbers of turns the corrosion properties of the samples are improved. This is attributed to the evolution of the microstructure into the more uniform grain refinement and distribution with fewer turns of HPT as shown in Figure 1. The uniformity of mechanical properties and texture as a result of the uniformity of microstructure of ZK60 with saturation in grain refinement at high numbers of turns of HPT was studied extensively in earlier investigations of the authors [27,41]. As described earlier, higher numbers of N results in saturation of grain refinement, refined grains distributed homogeneously on entire of the surfaces and consequently it minimizes the occurrence of micro-galvanic cells and ultimately leads to an improved corrosion resistance on these samples. Furthermore, the appearance of a pseudo-passive potential in the potentiodynamic polarization corroborates this assumption. It was suggested that increasing the numbers of turns increases the integrity and protectivity of the surface film. Moreover, the inductive loop in the Nyquist spectra appears when the corrosion products are fragmented [21,87-89], and the dissolved Mg generates intermediate species which remain adsorbed but unstable on the surface. The shrinking inductive loop and appearance of a diffusion

impedance through corrosion product in the Nyquist spectra also confirms this proposal [55,58,60]. In addition, as illustrated in the Mott-Schottky test in Figure 8 and the EDS results in Table 2, a preferable protective film with fewer defects was achieved in the oxide film by further homogenizing and refining the microstructure.

In the microscopic corrosion morphologies in Fig 13, islands of cracked corrosion products are gradually replaced with uniform compact oxide films with increasing numbers of HPT turns. Plastic deformation creates many lattice defects, interstitials and vacancies [21], and in addition more grain boundaries with lower atomic densities are produced compared to within the grains [75,76]. Recent studies show nano-sized second phase precipitation from the highly supersaturated Mg matrix [5,83,86] may form during the HPT process. These distributed defects, refined grains and precipitates potentially react with the solution and become oxidized more rapidly throughout the whole area of the disk simultaneously[9]. Thus, HPT samples with higher turns exhibit uniform corrosion because of the uniform distribution of grains, second phases and oxide film and as a result there is less occurrence of micro-galvanic cells.

Processing route is also another key factor affecting on corrosion response in addition to grain size and grain size distribution dependency [5]. The textural analysis with pole figures from the surfaces of the disks prepared for corrosion tests demonstrated an evolution of grain orientation at the surface of the disks from extruded materials with prismatic planes parallel to the surfaces to a final basal {0001} fiber texture with the c-axis parallel to the ND after processing by 5 turns of HPT. In Mg alloys, the basal planes have a slower oxidation rate compared to the prismatic planes due to their higher densities and order of atoms [44,91-93].

It should be noted that it is not possible to isolate the effect of texture and grain size on the overall corrosion behavior of the HPT-processed samples. Nevertheless, at high numbers of HPT

turns with more uniformity, it is reasonable to assume that this change in crystal structure and orientation of the samples also plays a significant role in the observed results with the corrosion behavior of the samples improved after 5 turns.

5. Summary and conclusions

The microstructural evolution and its influence on the electrochemical behavior of extruded and HPT-processed ZK60 alloy were investigated in this study. In the early stages of HPT, applying straining leads to an inhomogeneous grain refinement and decreases the corrosion resistance of this alloy. Applying more rotations improves the uniformity of the grains and the grain size distribution. The uniform and finely distributed grains can effectively decrease the corrosion activity through rapid formation of a smooth oxide film at the grain boundaries and surface crystalline defects. Otherwise, grain refinement may cause inhomogeneities which will accelerate the dissolution process. In addition, an anisotropic texture was developed by increasing the numbers of turns and this could potentially improve the oxidation resistance of the disks. It should be emphasized that all experiments were conducted in a 0.1 M NaCl solution and, due to the nature of the Mg alloy oxide films, the results may vary in other environments.

References

- [1] K. Gusieva, C.H.J. Davies, J.R. Scully, N. Birbilis, Corrosion of magnesium alloys: the role of alloying, *Int. Mater. Rev.* 60 (2015) 169–194.
- [2] A. Atrens, S. Johnston, Z. Shi, M.S. Dargusch, *Scripta Materialia Viewpoint - Understanding Mg corrosion in the body for biodegradable medical implants* Sputter deposited alloys Ultra-high purity Mg, *Scr. Mater.* 154 (2018) 92–100.

- [3] B.A. Atrens, G. Song, M. Liu, Z. Shi, F. Cao, M.S. Dargusch, Review of Recent Developments in the Field of Magnesium Corrosion, (2015).
- [4] J. Chen, L. Tan, K. Yang, Effect of heat treatment on mechanical and biodegradable properties of an extruded ZK60 alloy, *Bioact. Mater.* 2 (2017) 19–26.
- [5] D. Orlov, K.D. Ralston, N. Birbilis, Y. Estrin, Enhanced corrosion resistance of Mg alloy ZK60 after processing by integrated extrusion and equal channel angular pressing, *Acta Mater.* 59 (2011) 6176–6186.
- [6] D. Song, A. Ma, J. Jiang, P. Lin, D. Yang, J. Fan, Corrosion behavior of equal-channel-angular-pressed pure magnesium in NaCl aqueous solution, *Corros. Sci.* 52 (2010) 481–490.
- [7] D. Song, A.B. Ma, J.H. Jiang, P.H. Lin, D.H. Yang, J.F. Fan, Corrosion behaviour of bulk ultra-fine grained AZ91D magnesium alloy fabricated by equal-channel angular pressing, *Corros. Sci.* 53 (2011) 362–373.
- [8] R. Xin, Y. Luo, A. Zuo, J. Gao, Q. Liu, Texture effect on corrosion behavior of AZ31 Mg alloy in simulated physiological environment, *Mater. Lett.* 72 (2012) 1–4.
- [9] C.L.P. Silva, A.C. Oliveira, C.G.F. Costa, R.B. Figueiredo, M. deF. Leite, M.M. Pereira, V.F.C. Lins, T.G. Langdon, Effect of severe plastic deformation on the biocompatibility and corrosion rate of pure magnesium, *J. Mater. Sci.* 52 (2017) 5992–6003.
- [10] D. Ahmadkhaniha, Y. Huang, M. Jaskari, A. Järvenpää, M.H. Sohi, C. Zanella, L.P. Karjalainen, T.G. Langdon, Effect of high-pressure torsion on microstructure, mechanical properties and corrosion resistance of cast pure Mg, *J. Mater. Sci.* 53 (2018) 16585–16597.
- [11] C. By, N. Birbilis, Y. Estrin, Corrosion of Pure Mg as a Function of Grain Size and Processing Route, *Adv. Eng. Mater.* 10 (2008) 579–582.

- [12] D. Song, C. Li, N. Liang, F. Yang, J. Jiang, J. Sun, G. Wu, A. Ma, X. Ma, Simultaneously improving corrosion resistance and mechanical properties of a magnesium alloy via equal-channel angular pressing and post water annealing, *Mater. Des.* 166 (2019) 107621.
- [13] K.D. Ralston, N. Birbilis, C.H.J. Davies, Revealing the relationship between grain size and corrosion rate of metals, *Scr. Mater.* 63 (2010) 1201–1204.
- [14] S. Gollapudi, Grain size distribution effects on the corrosion behaviour of materials, *Corros. Sci.* 62 (2012) 90–94.
- [15] M. Hoseini, A. Shahryari, S. Omanovic, J.A. Szpunar, Comparative effect of grain size and texture on the corrosion behaviour of commercially pure titanium processed by equal channel angular pressing, *Corros. Sci.* 51 (2009) 3064–3067.
- [16] H.S. Kim, W.J. Kim, Enhanced corrosion resistance of ultrafine-grained AZ61 alloy containing very fine particles of $Mg_{17}Al_{12}$ phase, *Corros. Sci.* 75 (2013) 228–238.
- [17] Y. Huang, R.B. Figueiredo, T. Baudin, F. Brisset, T.G. Langdon, Evolution of strength and homogeneity in a magnesium AZ31 alloy processed by high-pressure torsion at different temperatures, *Adv. Eng. Mater.* 14 (2012) 1018–1026.
- [18] R.B. Figueiredo, T.G. Langdon, Processing Magnesium and Its Alloys by High-Pressure Torsion : An Overview, 1801039 (2018) 1–15.
- [19] J. Jayaraj, S. Amruth Raj, A. Srinivasan, S. Ananthakumar, U.T.S. Pillai, N.G.K. Dhaipule, U.K. Mudali, Composite magnesium phosphate coatings for improved corrosion resistance of magnesium AZ31 alloy, *Corros. Sci.* 113 (2016) 104–115.
- [20] S. Pawar, T.J.A. Slater, T.L. Burnett, X. Zhou, G.M. Scamans, Z. Fan, G.E. Thompson, P.J. Withers, Crystallographic effects on the corrosion of twin roll cast AZ31 Mg alloy sheet, *Acta Mater.* 133 (2017) 90–99.

- [21] Q. Liu, Q.X. Ma, G.Q. Chen, X. Cao, S. Zhang, J.L. Pan, G. Zhang, Q.Y. Shi, Enhanced corrosion resistance of AZ91 magnesium alloy through refinement and homogenization of surface microstructure by friction stir processing, *Corros. Sci.* 138 (2018) 284–296.
- [22] J.H. Gao, S.K. Guan, Z.W. Ren, Y.F. Sun, S.J. Zhu, B. Wang, Homogeneous corrosion of high pressure torsion treated Mg–Zn–Ca alloy in simulated body fluid, *Mater. Lett.* 65 (2011) 691–693.
- [23] C.Z. Zhang, S.J. Zhu, L.G. Wang, R.M. Guo, G.C. Yue, S.K. Guan, Microstructures and degradation mechanism in simulated body fluid of biomedical Mg–Zn–Ca alloy processed by high pressure torsion, *Mater. Des.* 96 (2016) 54–62.
- [24] B.C. Zhang, S. Guan, L. Wang, S. Zhu, J. Wang, R. Guo, Effect of Solution Pretreatment on Homogeneity and Corrosion Resistance of Biomedical Mg – Zn – Ca Alloy Processed by High Pressure Torsion, *Adv. Eng. Mater.* (2016) 1–11.
- [25] X. Wang, M. Nie, C.T. Wang, S.C. Wang, N. Gao, Microhardness and corrosion properties of hypoeutectic Al-7Si alloy processed by high-pressure torsion, *Mater. Des.* 83 (2015) 193–202.
- [26] K. Bryła, J. Morgiel, M. Faryna, K. Edalati, Z. Horita, Effect of high-pressure torsion on grain refinement, strength enhancement and uniform ductility of EZ magnesium alloy, *Mater. Lett.* 212 (2018) 323–326.
- [27] S.A. Torbati-Sarraf, T.G. Langdon, Properties of a ZK60 magnesium alloy processed by high-pressure torsion, *J. Alloy. Compd.* 613. (2014) 357–363.
- [28] S.A. Torbati-Sarraf, R. Alizadeh, R. Mahmudi, T.G. Langdon, Evaluating the flow properties of a magnesium ZK60 alloy processed by high-pressure torsion: A comparison of two different miniature testing techniques, *Mater. Sci. Eng. A* 708 (2017) 432–439.

- [29] S. Sabbaghianrad, S.A. Torbati-Sarraf, T.G. Langdon, An investigation of the limits of grain refinement after processing by a combination of severe plastic deformation techniques: A comparison of Al and Mg alloys, *Mater. Sci. Eng. A* 712 (2018) 373–379.
- [30] S.A. Torbati-Sarraf, S. Sabbaghianrad, T.G. Langdon, Microstructural properties, thermal stability and superplasticity of a ZK60 Mg alloy processed by high-pressure torsion, *Lett. Mater.* 5 (2015) 287–293.
- [31] S.A. Torbati-Sarraf, S. Sabbaghianrad, T.G. Langdon, Using post-deformation annealing to optimize the properties of a ZK60 magnesium alloy processed by high-pressure torsion, *Adv. Eng. Mater.* 20 (2017) 1-10.
- [32] R.B. Figueiredo, P.R. Cetlin, T.G. Langdon TG, Using finite element modeling to examine the flow processes in quasi-constrained high-pressure torsion. *Mater. Sci. Eng. A* 528 (2011) 8198-8204.
- [33] S.A. Torbati-Sarraf, S. Sabbaghianrad, R.B. Figueiredo, T.G. Langdon, Orientation imaging microscopy and microhardness in a ZK60 magnesium alloy processed by high-pressure torsion, *J. Alloys Compd.* 712 (2017) 185–193.
- [34] C.L.P. Silva, I.C. Tristão, S. Sabbaghianrad, S.A. Torbati-Sarraf, R.B. Figueiredo, T.G. Langdon, Microstructure and hardness evolution in magnesium processed by HPT, *Mater. Res.* 20 (2017) 2-7.
- [35] D.S.J. G.L. Song, A. Atrens, An Hydrogen Evolution Method for the Estimation of the Corrosion Rate of Magnesium Alloys, *Magnes. Technol.* (2001) 565–572.
- [36] S. Fajardo, G.S. Frankel, Gravimetric method for hydrogen evolution measurements on dissolving magnesium, *J. Electrochem. Soc.* 162 (2015) C693–C701.

- [37] M. Esmaily, J.E. Svensson, S. Fajardo, N. Birbilis, G.S. Frankel, S. Virtanen, R. Arrabal, S. Thomas, L.G. Johansson, Fundamentals and advances in magnesium alloy corrosion, *Prog. Mater. Sci.* 89 (2017) 92–193.
- [38] M. Liu, P. Schmutz, P.J. Uggowitzer, G. Song, A. Atrens, The influence of yttrium (Y) on the corrosion of Mg – Y binary alloys, *Corros. Sci.* 52 (2010) 3687–3701.
- [39] G. Song, A. Atrens, Understanding magnesium corrosion. A framework for improved alloy performance, *Adv. Eng. Mater.* 5 (2003) 837–858.
- [40] X. Mn, F. Cao, Z. Shi, G. Song, M. Liu, A. Atrens, B. Sem, Corrosion behaviour in salt spray and in 3 . 5 % NaCl solution saturated with Mg (OH)₂ of as-cast and solution heat-treated binary Mg – X alloys : X = Mn, Sn, Ca, Zn, Al, Zr, Si, Sr , *Corros. Sci.* 76 (2013) 60–97.
- [41] H.J. Lee, S.K. Lee, K.H. Jung, G.A. Lee, B. Ahn, M. Kawasaki, T.G. Langdon, Evolution in hardness and texture of a ZK60A magnesium alloy processed by high-pressure torsion, *Mater. Sci. Eng. A* 630 (2015) 90–98.
- [42] Y. Huang, R.B. Figueiredo, T. Baudin, A.L. Helbert, F. Brisset, T.G. Langdon, Effect of temperature on the processing of a magnesium alloy by high-pressure torsion, *J. Mater. Sci.* 47 (2012) 7796–7806.
- [43] S. Fajardo, C.F. Glover, G. Williams, G.S. Frankel, The Source of Anodic Hydrogen Evolution on Ultra High Purity Magnesium, *Electrochim. Acta.* 212 (2016) 510–521.
- [44] K. Hagihara, M. Okubo, M. Yamasaki, T. Nakano, Crystal-orientation-dependent corrosion behaviour of single crystals of a pure Mg and Mg-Al and Mg-Cu solid solutions, *Corros. Sci.* 109 (2016) 68–85.
- [45] Y. Song, E.H. Han, D. Shan, C.D. Yim, B.S. You, The effect of Zn concentration on the corrosion behavior of Mg-xZn alloys, *Corros. Sci.* 65 (2012) 322–330.

- [46] G.L. Song, A. Atrens, Corrosion mechanisms of magnesium alloys, *Adv. Eng. Mater.* 1 (1999) 11–33.
- [47] Z. Shi, M. Liu, A. Atrens, Measurement of the corrosion rate of magnesium alloys using Tafel extrapolation, *Corros. Sci.* 52 (2010) 579–588.
- [48] G.S. Frankel, A. Samaniego, N. Birbilis, Evolution of hydrogen at dissolving magnesium surfaces, *Corros. Sci.* 70 (2013) 104–111.
- [49] M. Curioni, F. Scenini, T. Monetta, F. Bellucci, Correlation between electrochemical impedance measurements and corrosion rate of magnesium investigated by real-time hydrogen measurement and optical imaging, *Electrochim. Acta* 166 (2015) 372–384.
- [50] G. Song, A. Atrens, D. Stjohn, J. Nairn, Y. Li, The electrochemical corrosion of pure magnesium in 1 N NaCl, *Corros. Sci.* 39 (1997) 855–875.
- [51] G. Song, A. Atrens, D.S. John, X. Wu, J. Nairn, The anodic dissolution of magnesium in chloride and sulphate solutions, *Corros. Sci.* 39 (1997) 1981–2004.
- [52] N. Causse, S. Leleu, B. Rives, On the stability of the oxides film formed on a magnesium alloy containing rare-earth elements, *Electrochim. Acta.* 290 (2018) 586–594.
- [53] A.D. King, N. Birbilis, J.R. Scully, Accurate Electrochemical Measurement of Magnesium Corrosion Rates; a Combined Impedance , Mass-Loss and Hydrogen Collection Study, *Electrochim. Acta.* 121 (2014) 394–406.
- [54] G. Baril, G. Galicia, C. Deslouis, N. Pébère, B. Tribollet, V. Vivier, An impedance investigation of the mechanism of pure magnesium corrosion in sodium sulfate solutions, *J. Electrochem. Soc.* 154 (2007) C108-C113.
- [55] G. Baril, N. Pébère, The corrosion of pure magnesium in aerated and deaerated sodium sulphate solutions, *Corros. Sci.* 43 (2001) 471–484.

- [56] J. Chen, J. Wang, E. Han, J. Dong, W. Ke, AC impedance spectroscopy study of the corrosion behavior of an AZ91 magnesium alloy in 0.1 M sodium sulfate solution, *Electrochim. Acta.* 52 (2007) 3299–3309.
- [57] W. Davidson, J. Kleinberg, R.L. Petty, W. Davidson, The Anodic Oxidation of Magnesium Metal : Evidence for the Existence of Unipositive, *J. Am. Chem. Soc.* 2 (1954) 368.
- [58] G. Galicia, N. Pébère, B. Tribollet, V. Vivier, Local and global electrochemical impedances applied to the corrosion behaviour of an AZ91 magnesium alloy, *Corros. Sci.* 51 (2009) 1789–1794.
- [59] G.G. Perrault, The potential-pH diagram of the magnesium-water system, *J. Electroanal. Chem. Interfacial Electrochem.* 51 (1974) 107–119.
- [60] G. Baril, C. Blanc, N. Pébère, AC Impedance Spectroscopy in Characterizing Time-Dependent Corrosion of AZ91 and AM50 Magnesium Alloys Characterization with Respect to Their Microstructures, *J. Electrochem. Soc.* 148 (2001) B489.
- [61] B. Tribollet, G. Galicia, N. Pebere, V. Vivier, Corrosion Study of an AZ91 Magnesium alloy by EIS and LEIS, *ECS Trans.*, ECS, 2006: pp. 157–168.
- [62] G.J. Brug, A.L.G. van den Eeden, M. Sluyters-Rehbach, J.H. Sluyters, The analysis of electrode impedances complicated by the presence of a constant phase element, *J. Electroanal. Chem. Interfacial Electrochem.* 176 (1984) 275–295.
- [63] M. Musiani, M.E. Orazem, N. Pébère, B. Tribollet, V. Vivier, Constant-Phase-Element Behavior Caused by Coupled Resistivity and Permittivity Distributions in Films, *J. Electrochem. Soc.* 158 (2011) C424.
- [64] J.B. Jorcin, M.E. Orazem, N. Pébère, B. Tribollet, CPE analysis by local electrochemical impedance spectroscopy, *Electrochim. Acta.* 51 (2006) 1473–1479.

- [65] C.H. Hsu, F. Mansfeld, Technical Note : Concerning the Conversion of the Constant Phase Element Parameter Y_0 into a Capacitance, *Corrosion*. 57 (2001) 747–748.
- [66] M. Benoit, C. Bataillon, B. Gwinner, F. Miserque, M.E. Orazem, C.M. Sánchez-sánchez, B. Tribollet, V. Vivier, Comparison of different methods for measuring the passive film thickness on metals, *Electrochim. Acta*. 201 (2016) 340–347.
- [67] S. Chakri, I. Frateur, M.E. Orazem, E.M.M. Sutter, T.T.M. Tran, B. Tribollet, V. Vivier, Improved EIS Analysis of the Electrochemical behavior of carbon Steel in Alkaline solution, *Electrochim. Acta*. 246 (2017) 924–930.
- [68] A. Son, N. Causse, M. Musiani, M.E. Orazem, N. Pébère, B. Tribollet, V. Vivier, Determination of water uptake in organic coatings deposited on 2024 aluminium alloy : Comparison between impedance measurements and gravimetry, *Prog. Org. Coatings*. 112 (2017) 93–100.
- [69] A.K. Jonscher, Dielectric characterisation of semiconductors, *Solid. State. Electron*. 33 (1990) 737–742.
- [70] T. Zhang, Y. Shao, G. Meng, Y. Li, F. Wang, Effects of hydrogen on the corrosion of pure magnesium, 52 (2006) 1323–1328.
- [71] D.D. Macdonald, The history of the point defect model for the passive state: a brief review of film growth aspects, *Electrochim. Acta* 56 (2011) 1761-1772.
- [72] K. Darowicki, S. Krakowiak, P. Slepiski, Selection of measurement frequency in Mott – Schottky analysis of passive layer on nickel, *Electrochim. Acta*. 51 (2006) 2204–2208.
- [73] X. Liu, T. Zhang, Y. Shao, G. Meng, F. Wang, Effect of alternating voltage treatment on the corrosion resistance of pure magnesium, *Corros. Sci.* 51 (2009) 1772-1779.

- [74] J. Chen, J. Wang, E. Han, J. Dong, W. Ke, States and transport of hydrogen in the corrosion process of an AZ91 magnesium alloy in aqueous solution, *Corros. Sci.* 50 (2008) 1292–1305.
- [75] M.C.L. de Oliveira, V.S.M. Pereira, O.V. Correa, N.B. de Lima, R.A. Antunes, Correlation between the corrosion resistance and the semiconducting properties of the oxide film formed on AZ91D alloy after solution treatment, *Corros. Sci.* 69 (2013) 311–321.
- [76] D.D. Macdonald, The point defect model for the passive state, *J. Electrochem. Soc.* 139 (1992) 3434–3449.
- [77] M.H. Dean, U. Stimming, The electronic properties of disordered passive films, *Corros. Sci.* 29 (1989) 199–211.
- [78] K.L. Merkle, D.J. Smith, Atomic structure of symmetric tilt grain boundaries in NiO, *Phys. Rev. Lett.* 59 (1987) 2887–2890.
- [79] M. Wagner, Structure and thermodynamic properties of nanocrystalline metals, *Am. Phys. Soc.* 45 (1992) 635–640.
- [80] V. Afshari, C. Dehghanian, Effects of grain size on the electrochemical corrosion behaviour of electrodeposited nanocrystalline Fe coatings in alkaline solution, *Corros. Sci.* 51 (2009) 1844–1849.
- [81] Y.L. Cheng, T.W. Qin, H.M. Wang, Z. Zhang, Comparison of corrosion behaviors of AZ31, AZ91, AM60 and ZK60 magnesium alloys, *Trans. Nonferrous Met. Soc. China (English ed.)* 19 (2009) 517–524.
- [82] C.L.P. Silva, R.B. Soares, P.R. Pereira, R.B. Figueiredo, V.F.C. Lins, T.G. Landgon, The effect of high-pressure torsion on microstructure, hardness and corrosion behavior for pure magnesium and different magnesium alloys, *Adv. Eng. Mater.* DOI: 10.1002/adem.201801081.

- [83] W. Liu, F. Cao, Y. Xia, L. Chang, J. Zhang, Localized Corrosion of Magnesium Alloys in NaCl Solutions Explored by Scanning Electrochemical Microscopy in Feedback Mode, *Electrochim. Acta*. 132 (2014) 377–388.
- [84] E. Nationale, P. De Grenoble, Structure and deformation behavior of Armco iron subjected to severe plastic deformation, *Acta Mater.* 44 (1996) 4705–4712.
- [85] F. Wetscher, A. Vorhauer, R. Stock, R. Pippan, Structural refinement of low alloyed steels during severe plastic deformation, *Mater. Sci. Eng. A*. 389 (2004) 809–816.
- [86] K. Edalati, D. Akama, A. Nishio, S. Lee, Y. Yonenaga, J.M. Cubero-Sesin, Z. Horita, Influence of dislocation-solute atom interactions and stacking fault energy on grain size of single-phase alloys after severe plastic deformation using high-pressure torsion, *Acta Mater.* 69 (2014) 68–77.
- [87] G. Song, Z. Xu, Crystal orientation and electrochemical corrosion of polycrystalline Mg, *Corros. Sci.* 63 (2012) 100–112.
- [88] Y. Song, D. Shan, R. Chen, F. Zhang, E. Han, Biodegradable behaviors of AZ31 magnesium alloy in simulated body fluid, *Mater. Sci. Eng. C* 29 (2009) 1039–1045.
- [89] J. Li, Q. Jiang, H. Sun, Y. Li, Effect of heat treatment on corrosion behavior of AZ63 magnesium alloy in 3.5 wt.% sodium chloride solution, *Corros. Sci.* 111 (2016) 288–301.
- [90] B.B. Straumal, V. Pontikis, A.R. Kilmametov, A.A. Mazilkin, S.V. Dobatkin, B. Baretzky, Competition between precipitation and dissolution in Cu–Ag alloys under high pressure torsion, *Acta Mater.* 122 (2017) 60–71.
- [91] L.G. Bland, K. Gusieva, J.R. Scully, Effect of crystallographic orientation on the corrosion of magnesium: comparison of film forming and bare crystal facets using electrochemical impedance and raman spectroscopy, *Electrochim. Acta* 227 (2017) 136–151.

- [92] X. Li, B. Jiang, J. He, J. Zhang, Z. Jiang, B. Liu, F. Pan, Improvement of planar isotropy, mechanical properties and corrosion resistance of extruded Mg-3Al-1Zn alloy sheet by special grain re-orientation, *J. Alloys Compd.* 72 (2017) 106–117.
- [93] M. Liu, D. Qiu, M. Zhao, A. Atrens, The effect of crystallographic orientation on the active corrosion of pure magnesium, *Scr. Mater.* 58 (2008) 421–424.

Legends:

Figure 1. Grain size distributions and EBSD orientation micrographs taken from the mid-radius of the RD-TD planes of the extruded material and samples processed by 1 and 5 turns of HPT. The

color coded triangle is representative of the crystallographic orientation of corresponding colors in the EBSD orientation micrographs.

Figure 2. The pole figures of {0001} crystallographic orientation from the mid-radius of the RD-TD planes of the extruded, and HPT processed samples with 1 and 5 turns at 298 K.

Figure 3. Polarization curves of the ZK60 samples in 0.1 M NaCl solution, processed by extrusion and various numbers of HPT turns.

Figure 4. Nyquist plots of one of the ZK60 Mg samples in 0.1 M NaCl solution, processed by extrusion and various numbers of turns by HPT, solid lines indicate fitted curves.

Figure 5. Equivalent circuit constructed based on the interface reactions observed in the EIS spectrum for the extruded and the HPT-processed ZK60 samples in 0.1M NaCl.

Figure 6. Cole-Cole plots corresponding to EIS data at high frequencies presented in Figure 4.

Figure 7. The Mott–Schottky plots for the ZK60 samples processed by extrusion and various numbers of turns by HPT, immersed in 0.1 M NaCl for 4 hours.

Figure 8. Donor density of the ZK60 Mg alloy processed by extrusion and various numbers of turns by HPT, immersed in 0.1M NaCl for 4 hours. In X axis, the 0 number of HPT turns represents the original extruded material with no HPT process.

Figure 9. Cumulative hydrogen evolution for extruded and HPT proceeded samples immersed in 0.1 M NaCl solution for 24 hours.

Figure 10. The optical images of the corroded surfaces of the extruded as well as HPT proceeded ZK60 samples at different immersion time (the diameter of each disk is ~10 mm).

Figure 11. The micrographs from slice of the 4 hours corroded surface of disks shown in Figure 10 for (a) extruded and processed by (b) 1, (c) 2, (d) 5, (e) 10 and (f) 20 turns of HPT.

Figure 12. The micrographs of the corroded surfaces of ZK60 Mg alloy samples at exposed in 0.1 M NaCl for 4 hours for (a) extruded and processed by (b) 1, (c) 2, (d) 5, (e) 10 and (f) 20 turns of HPT.

Figure 13. Fig. 12. SEM of surface morphologies of the ZK60 disks after 24 hours immersion in 0.1 M NaCl solution for samples of (a) extruded with point A for EDS analysis and processed by (b) 1 turn of HPT with point B for EDS analysis, (c) 2 turns of HPT with point, (d) 5 turns of HPT, (e) 10 turns of HPT and (f) 20 turns of HPT with point C for EDS analysis. The corresponding EDS results of point A, B and C are compared in Table 2.

Table 1. Results from the fitted EIS data in the equivalent circuits suggested in Figure. 5

Table 2. EDS results of corresponding areas in Figure. 11

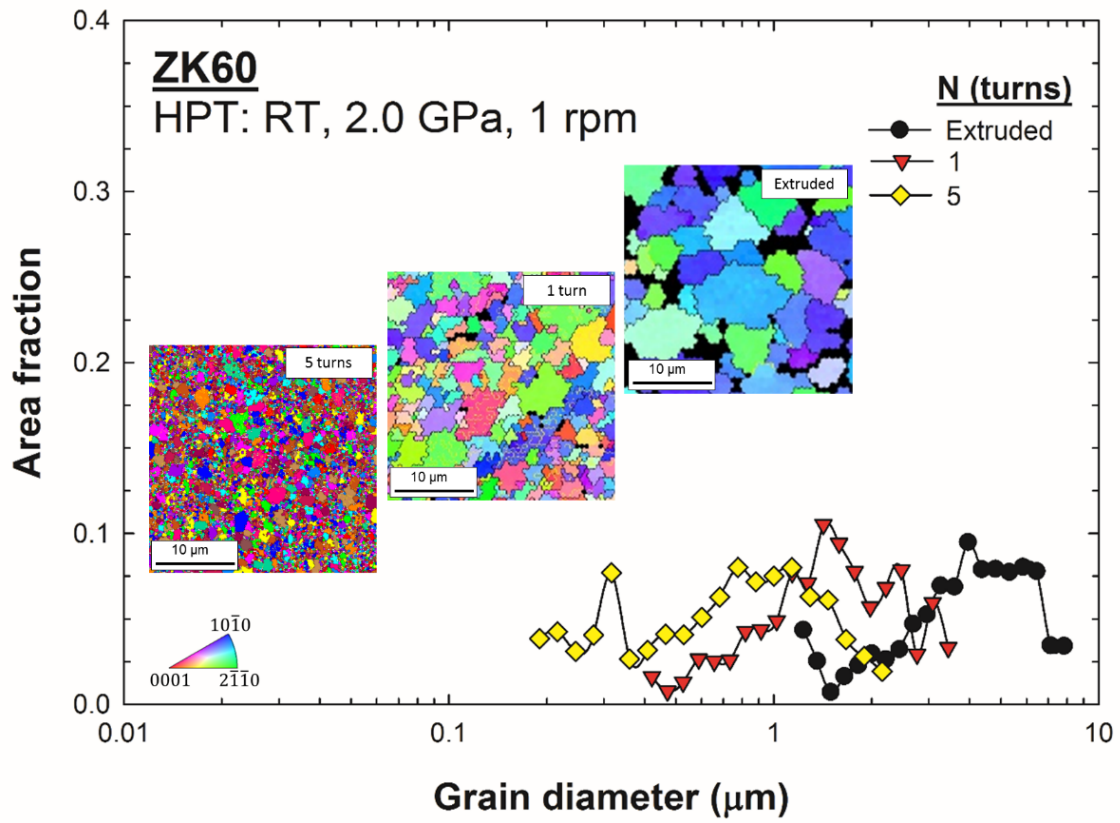


Fig. 1. Grain size distributions and EBSD orientation micrographs taken from the mid-radius of the RD-TD planes of the extruded material and samples processed by 1 and 5 turns of HPT. The color coded triangle is representative of the crystallographic orientation of corresponding colors in the EBSD orientation micrographs.

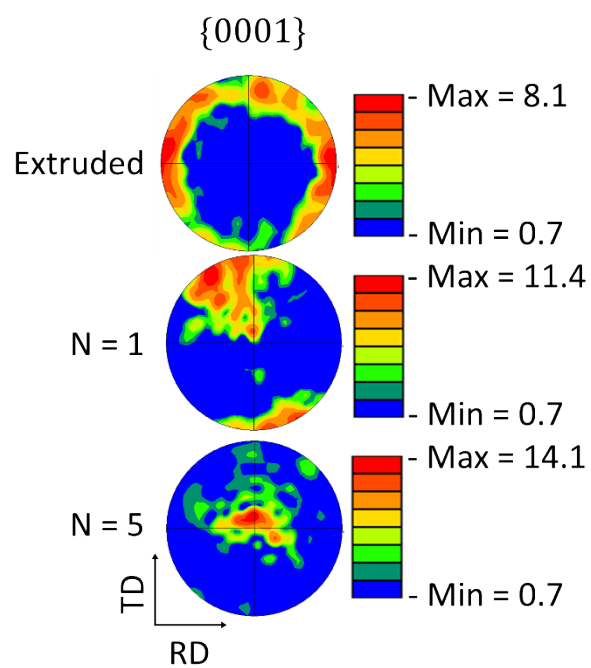


Fig. 2. The pole figures of $\{0001\}$ crystallographic orientation from the mid-radius of the RD-TD planes of the extruded, and HPT processed samples with 1 and 5 turns at 298 K.

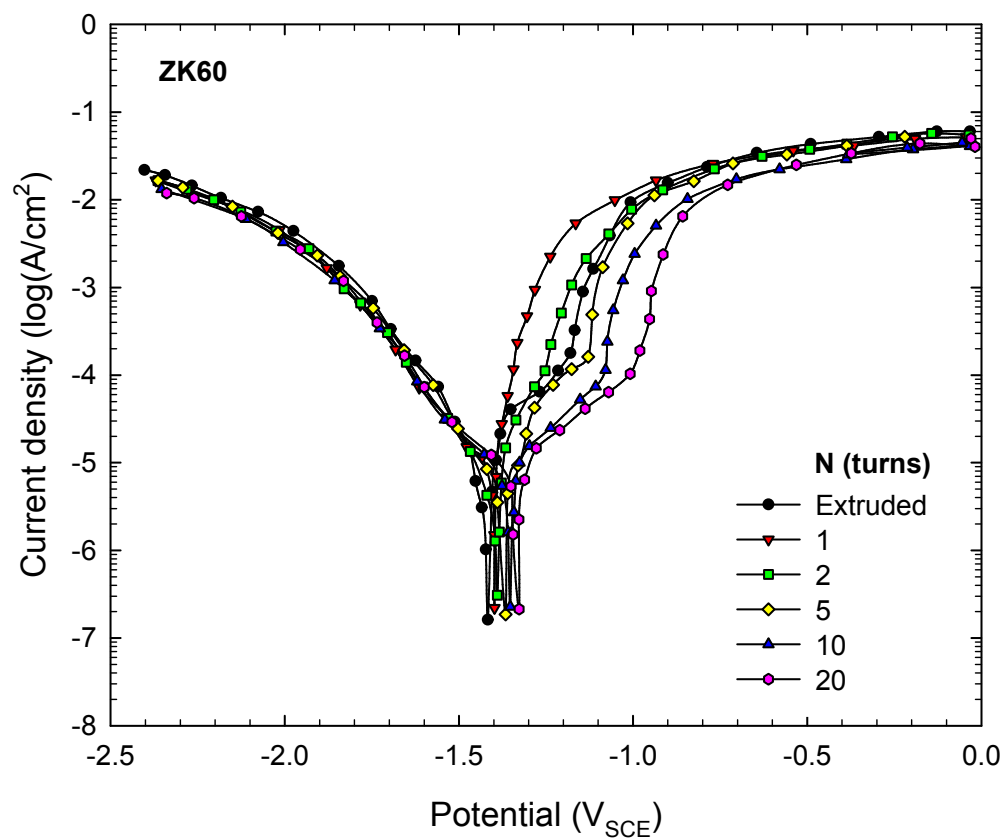


Fig. 3. Polarization curves of the ZK60 samples in 0.1 M NaCl solution, processed by extrusion and various numbers of HPT turns.

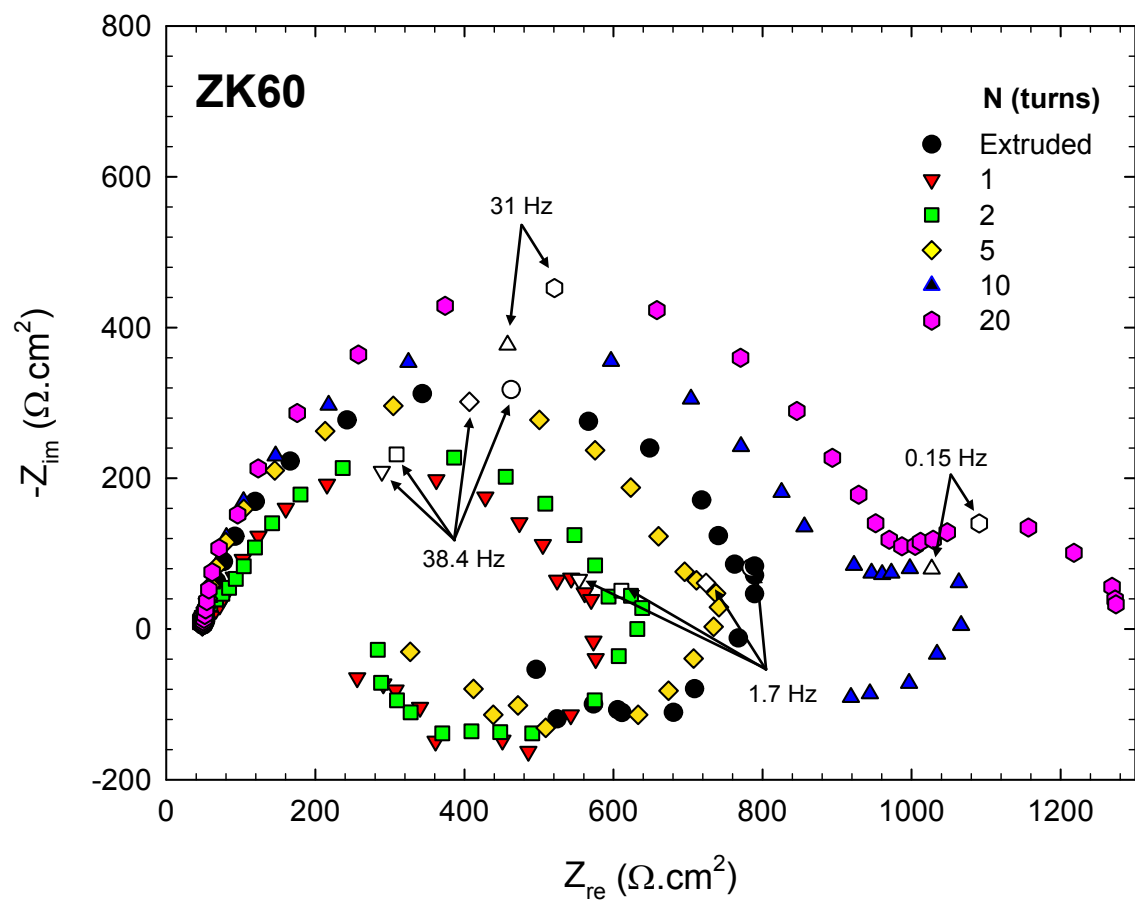


Fig. 4. Nyquist plots of one of the ZK60 Mg samples in 0.1 M NaCl solution, processed by extrusion and various numbers of turns by HPT.

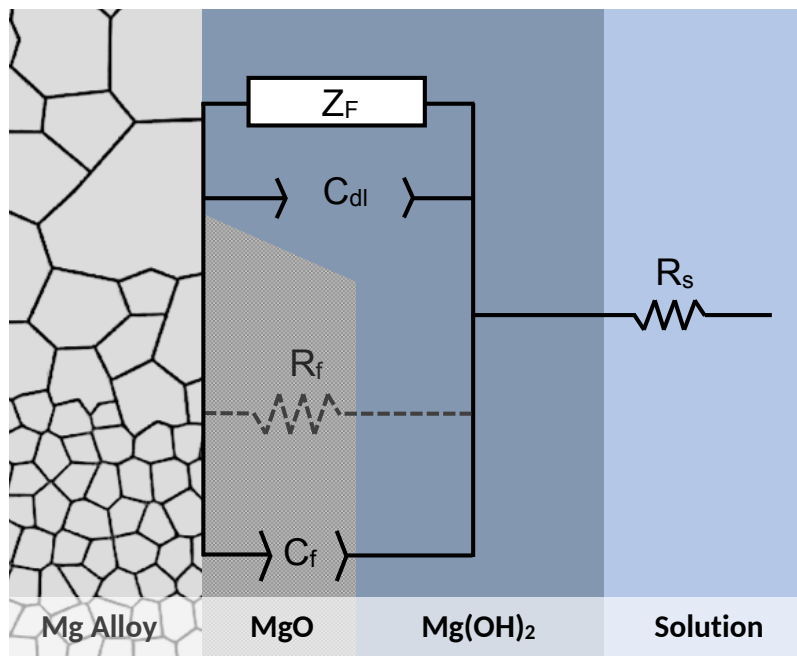


Fig. 5. Equivalent circuit constructed based on the interface reactions observed in the EIS spectrum for the extruded and the HPT processed ZK60 samples in 0.1 M NaCl.

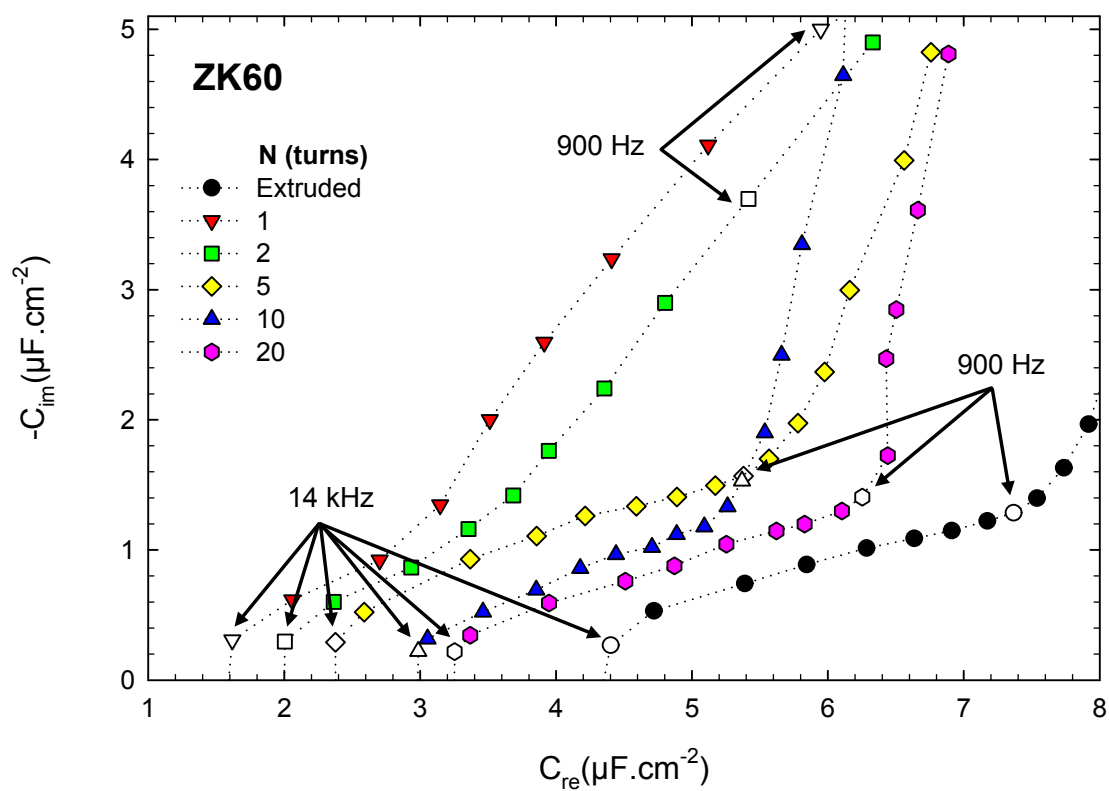


Fig. 6. Cole-Cole plots corresponding to EIS data at high frequencies presented in Figure 4.

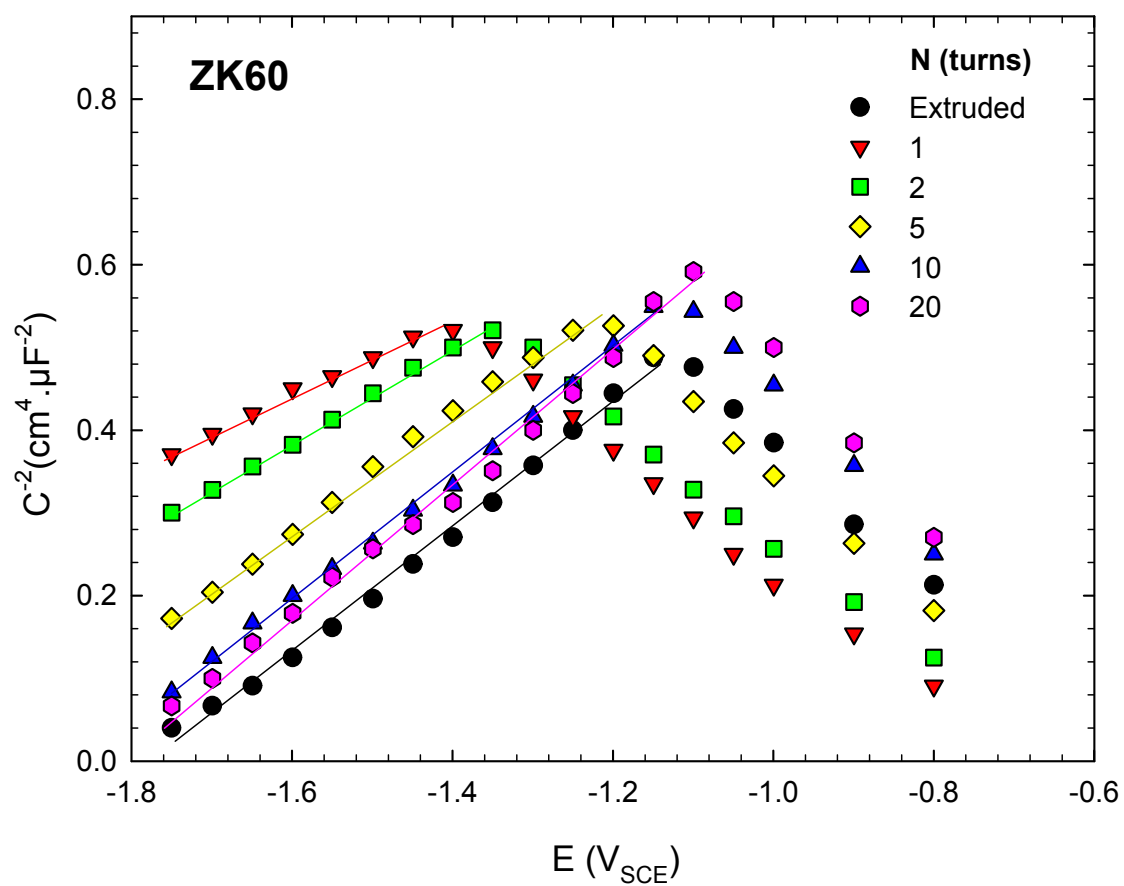


Fig. 7. The Mott-Schottky plots for the ZK60 samples processed by extrusion and various numbers of turns by HPT, immersed in 0.1 M NaCl for 4 hours.

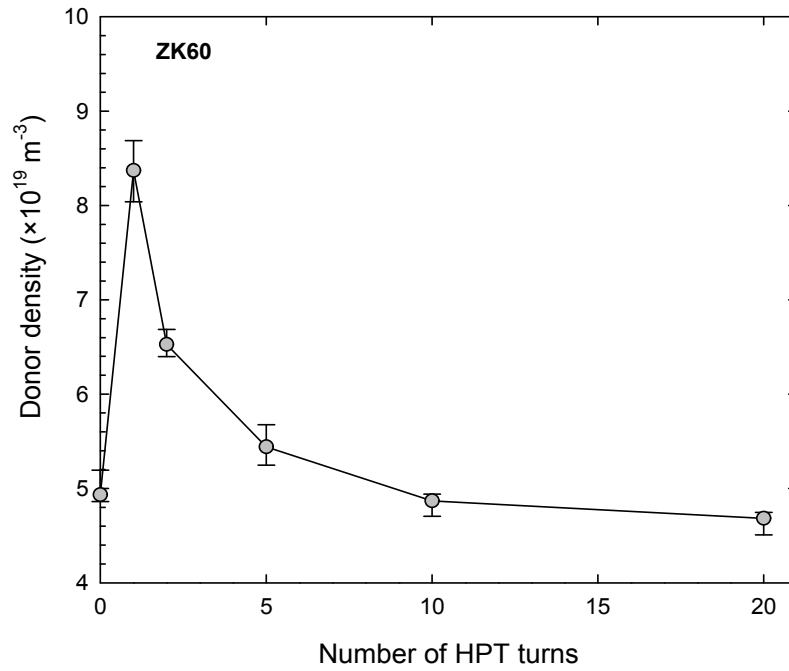


Fig. 8. Donor density of the ZK60 Mg alloy processed by extrusion and various numbers of turns by HPT, immersed in 0.1 M NaCl for 4 hours. In X axis, the 0 number of HPT turns represents the original extruded material with no HPT process.

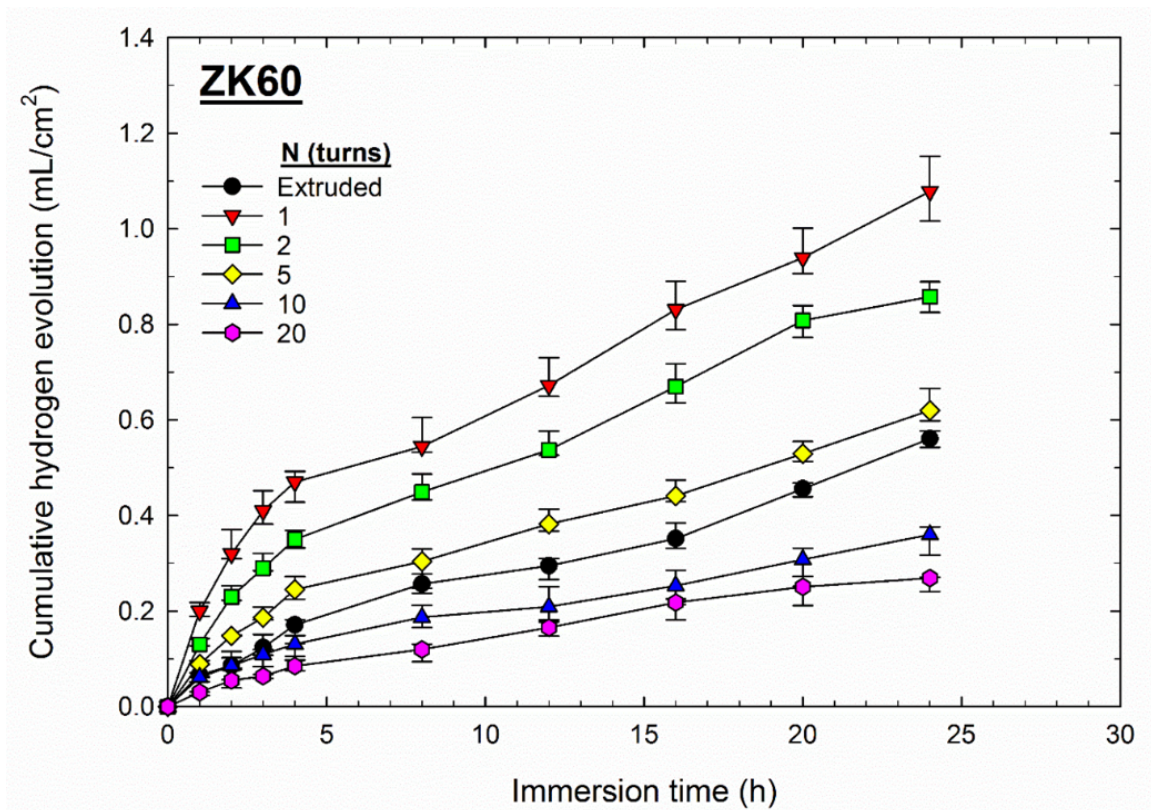


Fig. 9. Cumulative hydrogen evolution for extruded and HPT proceeded samples immersed in 0.1 M NaCl solution for 24 hours.

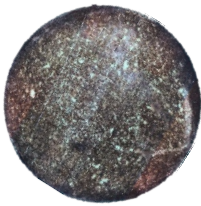
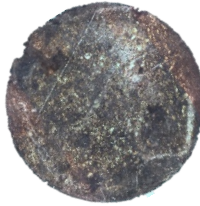



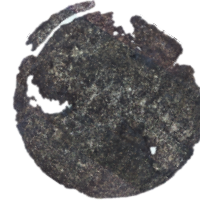
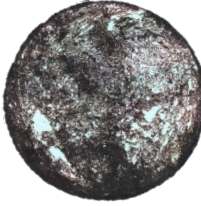
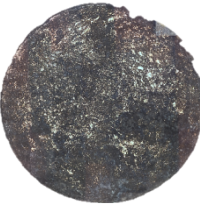

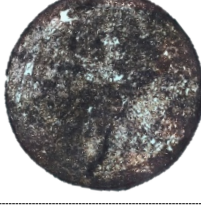


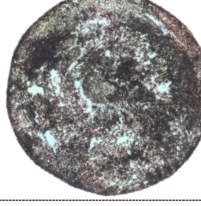
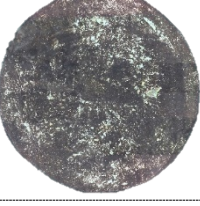
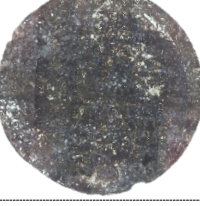
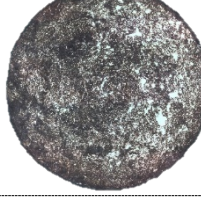
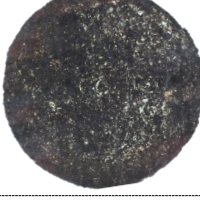

<u>N(turns)</u>	Hours of exposure		
	4	10	24
Extruded			
1			
2			
5			
10			
20			

Fig. 10. The optical images of the corroded surfaces of the extruded as well as HPT proceeded ZK60 samples at different immersion time (the diameter of each disk is ~10 mm).

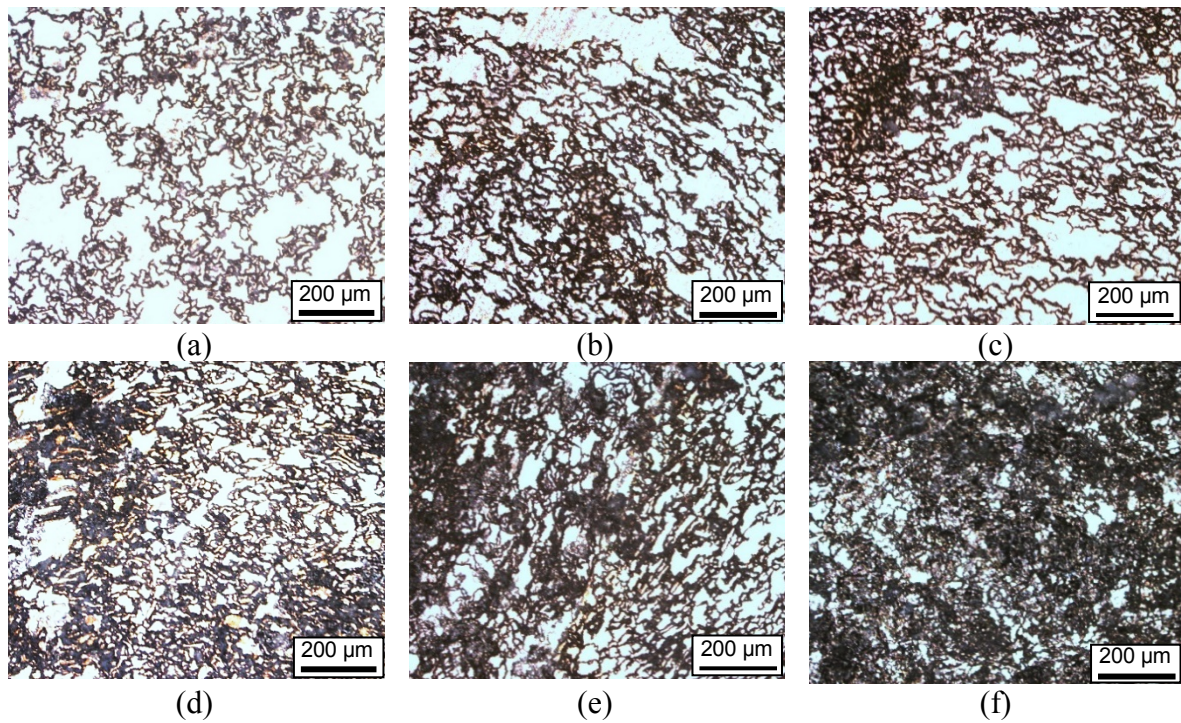


Fig. 11. The micrographs of the corroded surfaces of ZK60 Mg alloy samples at exposed in 0.1 M NaCl for 4 hours for (a) extruded and processed by (b) 1, (c) 2, (d) 5, (e) 10 and (f) 20 turns of HPT.

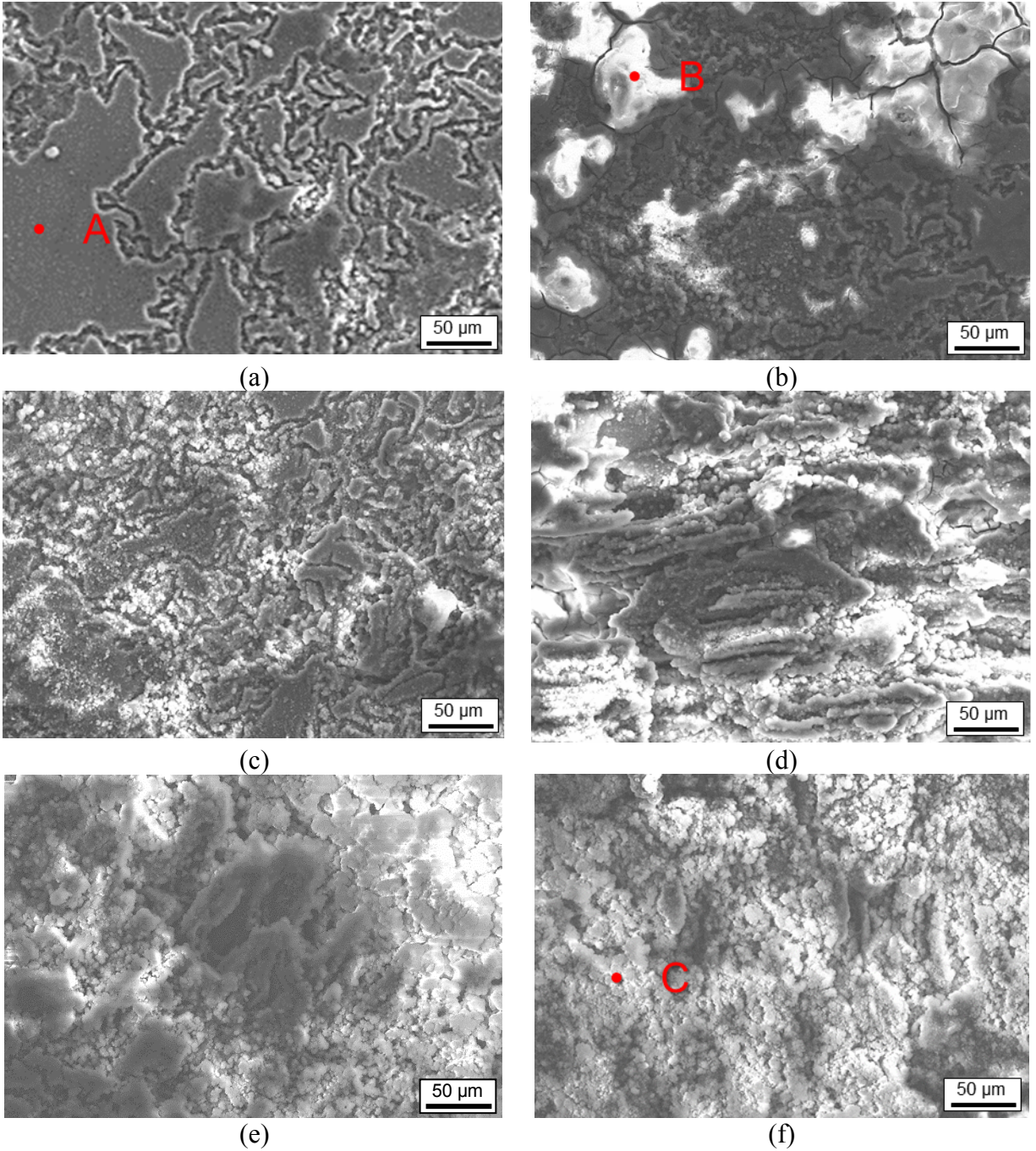


Fig. 12. SEM of surface morphologies of the ZK60 disks after 24 hours immersion in 0.1 M NaCl solution for samples of (a) extruded and processed by (b) 1 turn of HPT with point A for EDS analysis, (c) 2 turns of HPT with point B for EDS analysis, (d) 5 turns of HPT, (e) 10 turns of HPT and (f) 20 turns of HPT with point C for EDS analysis. The corresponding EDS results of point A, B and C are compared in Table 2.

Table 1. Results from the fitted EIS data in the equivalent circuits suggested in Figure 5

Sample	Extruded	1	2	5	10	20
$R_f(\Omega\text{cm}^2)$	760	510	590	680	870	980
$C_f(\mu\text{Fcm}^{-2})$	4.2	1.6	1.9	2.3	2.9	3.2

Table 2. EDS results of corresponding areas in Figure 11

Element (wt.%)	A	B	C
Mg	81.1	28.1	58.2
Zn	3.2	2.3	1.0
O	14.5	57.7	39.1
Cl	0.2	11.3	0.9